Istraživanja i projektovanja za privredu
ISSN 1451-4117
DOI:10.5937/jaes0-71332
www.engineeringscience.rs

iipp publishing

Journal of Applied Engineering Science
Original Scientific Paper,
Volume 24, Number 4, Year 2026,
no 1374, pp 827-839

EFFECT OF NODE PROTECTION ZONE ON THE CRASHWORTHINESS OF A BIOMIMETIC BAMBOO CRASH BOX UNDER AXIAL CRUSHING

Johan Wayan Dika[1], Moch. Agus Choiron[1]*, Putu Hadi Setyarini[1], Teguh Dwi Widodo[1], Yudhi Ariadi[2]

[1]Brawijaya University, Faculty of Engineering, Department of Mechanical Engineering, Malang, Indonesia
[2]University of Warwick, School of Engineering, Coventry, United Kingdom
**agus_choiron@ub.ac.id*

This study investigates the effect of the node protection zone on the crashworthiness of a biomimetic bamboo-inspired crash box under axial crushing. The node protection zone is defined using a dimensionless geometric coefficient, k_z, to characterize the spatial interaction between the node and the collapse-trigger region. Finite element simulations were performed using ANSYS Explicit Dynamics on a cylindrical crash box made of AlSi10Mg with a Johnson–Cook material model. The model configuration is defined by three main geometric parameters: node position (B), biomimetic void trigger density (C), and node protection zone coefficient (k_z). Three values of the node protection zone coefficient k_z =0,03, 0,05, and 0,07, were evaluated on a crash box with a diameter of 75 mm and a height of 100 mm. The results show that the B40-C4-Z05 configuration produced an energy absorption of 1,206.20 J and a mean crushing force of 13,215.30 N, representing increases of 31.64% and 31.63%, respectively, compared to the plain tube. This configuration also increased crush force efficiency and specific energy absorption by 36.62% and 11.84%, respectively, and reduced the initial peak force and maximum reaction force by 3.69% and 12.88%, respectively. The B40-C4-Z07 configuration produced a slightly lower initial peak force and a higher crush force efficiency than B40-C4-Z05, indicating a performance plateau between these configurations. Given that the 1.1% discrepancy in energy absorption between k_z=0,05 and k_z=0,07 is close to the numerical uncertainty threshold (0.81%), the results suggest that the performance stabilizes within this range. Within the design range studied k_z=0,05 to 0,07 offers a consistently optimized crashworthiness response with marginal sensitivity

Keywords: biomimetic crash box, node protection zone, crashworthiness, energy absorption, AlSi10Mg

HIGHLIGHTS

- A dimensionless node protection zone was developed for a biomimetic bamboo crash box.
- The k_z parameter characterized node–trigger interaction during axial crushing.
- The k_z = 0.05 configuration increased energy absorption by 31.64% compared with the plain tube.
- Node protection zone variation altered deformation, force response, and energy absorption.

1 Introduction

A crash box is one of the key components of a vehicle's passive safety system, designed to absorb and dissipate impact energy through controlled structural deformation. Finite-element studies of vehicle structures show that adding energy-absorbing elements to the front of a vehicle can reduce intrusion deformation while also lowering the force transmitted to the passenger compartment, thereby reinforcing the role of energy-absorbing structures in improving crash safety [1, 2].

Nevertheless, the effectiveness of a crash box depends not only on the presence of energy-absorbing elements, but also on the structural geometry's ability to control the location of deformation initiation, the sequence of folding, load distribution, and energy absorption efficiency. In this context, thin-walled structures (particularly tubular structures) have been widely developed as energy absorbers because they are capable of undergoing plastic buckling and progressive folding, which result in gradual energy dissipation [3]. Therefore, crashworthiness depends not only on material properties but also on the ability of structural geometry to direct and control the deformation and collapse mechanisms during axial loading. In numerical analysis, the structural response can also be influenced by the model configuration, boundary conditions, and modeling parameters used in finite element simulations; therefore, the selection and control of numerical parameters are an important part of parametric studies of structures undergoing deformation and collapse [4].

The biomimetic approach has emerged as a strategy for improving the performance of energy-absorbing structures by applying design principles found in biological structures. Bamboo is a particularly interesting source of inspiration because it has a hierarchical structure that combines high strength, stiffness, and structural efficiency [5, 6, 7]. Structurally, bamboo consists of relatively long internode segments and node elements that delimit and connect these segments. These characteristics result in a nonuniform distribution of stiffness along the stem and allow its mechanical response to occur gradually when subjected to a load [8]. A number of studies have incorporated these characteristics into energy-absorbing structures and have shown that bamboo-inspired configurations can improve

energy absorption (EA), specific energy absorption (SEA), and deformation stability compared to conventional tubular configurations [9, 10, 11].

One important characteristic that distinguishes bamboo structures from homogeneous thin-walled tubes is the presence of nodes. Biologically, nodes contribute to increased local stiffness and limit the propagation of damage along the stem, while the internode segments provide sections that are relatively more prone to deformation [12]. In the context of energy absorbers, this principle can be applied as a combination of deformation control elements (or deformation arrestors) and zones that allow for progressive deformation. A number of studies on bamboo-inspired structures have utilized nodal configurations to influence deformation patterns and energy absorption distribution [11, 13]. However, the presence of nodes as deformation-controlling elements also raises design issues when the location where failure initiates is not geometrically controlled relative to the node positions.

Controlling the initial collapse location is a critical aspect of crash box design because the location and sequence of crease formation can affect the initial peak force (IPF), force stability during the crushing process, and energy absorption efficiency. Therefore, various collapse-trigger strategies, such as grooves[14, 15], slots [16], bulkheads [13], and other local geometric modifications, have been developed to initiate deformation at specific locations. This strategy aims to reduce uncertainty regarding the location of the initial fold and produce a more controlled progressive folding mechanism. However, when a collapse trigger is applied to a structure that also contains nodal elements, the spatial relationship between the trigger and the nodes becomes an additional design factor that must be considered. The spatial position of the trigger relative to the node may influence the collapse behavior of the structure. A trigger located too close to the nodal region may interact strongly with the locally stiffened region, whereas a trigger located too far from the node may reduce the influence of the node on deformation localization. Therefore, the relative position between the node and the collapse trigger should be considered in the geometric design of the crash box.

Recent research on crashworthiness optimization indicates that controlling the interactions between local geometric features is becoming increasingly important. Previous studies have explored the effects of wall thickness [10], material distribution [17], lattice and auxetic filler configurations [18], origami patterns [19, 20], hybrid structures [21], and collapse trigger parameters using design of experiments [21], response surface methodology, and multi-objective optimization [15]. In bamboo-inspired structures, it has been shown that nodal elements and geometric configurations resembling the characteristics of bamboo can influence deformation mechanisms and energy absorption. On the other hand, research on collapse triggers indicates that modifications to local geometry can be used to direct the initiation of buckling and control the crushing response [22, 16]. Nevertheless, this approach generally treats nodes and triggers as separately designed geometric features. However, the spatial relationship between nodes and collapse triggers has not been explicitly formulated in the reviewed literature as a normalized geometric parameter that can be systematically varied to determine trigger locations. Unlike conventional geometric trigger-positioning approaches that rely on rigid, absolute-distance parameters or standalone optimization of a single feature, this study focuses on the coupled interaction between two opposing features: a localized stiffener (the node) and a localized softener (the trigger). Traditional methods often suffer from geometric scale-dependency, where absolute distances fail when the tube diameter changes.

This discrepancy highlights the need for a design parameter that can represent the node's influence zone on the location where deformation begins. This parameter is necessary not only to determine the geometric distance between the node and the trigger, but also to provide placement rules that can be reproduced when the dimensions of the crash box change. An absolute-distance-based approach can result in configurations that depend on the specific size of the structure, whereas parameters normalized to the structure's principal dimensions have the potential to provide a more consistent design basis. In this context, the node protection zone is used to define the region around a node that is kept free of collapse-triggering features. By defining these zones using dimensionless coefficients, the geometric relationship among the nodes, triggers, and principal crash-box dimensions of the crash box can be expressed geometrically.

Based on this gap, this study introduces the node protection zone as a geometric parameter to characterize and control the interaction between nodes, which function as deformation arrestors, and voids, which serve as collapse triggers, within a biomimetic bamboo-inspired crash box. Unlike approaches that merely vary the geometry of individual nodes or triggers, this study defines a node's influence region using the node protection zone coefficient, k_z, such that the size of the protection zone is expressed relative to the outer diameter of the crash box through the relationship.

$$Z = K_z D \tag{1}$$

where (Z) is the node protection zone and (D) is the outer diameter of the crash box. This dimensionless formulation is then used as the basis for determining the distance between the node center and the collapse trigger, and subsequently for determining the axial distribution of the trigger along the internode segment. Thus, the placement of the void is determined based on the geometric relationships linking the crash box dimensions, node positions, protection zones, and trigger locations, rather than solely through arbitrary geometric placement. The fundamental scientific contribution of this approach lies in treating the node's zone of influence as a distinct boundary constraint, mathematically ensuring that the initial plastic hinge formation is steered cleanly into the internode section without being structurally choked by the node's local rigidity.

This study further evaluates the effect of the node protection coefficient on crashworthiness response under axial loading. The evaluation was conducted by considering energy absorption (EA), initial peak force (IPF), mean crushing

force (MCF), crush force efficiency (CFE), and specific energy absorption (SEA), as well as the resulting progressive deformation characteristics. This evaluation was used to identify the relationship between the size of the node's protection zone, node–trigger interactions, and energy absorption mechanisms during the crushing process.

Thus, the main contribution of this study is the development of dimensionless geometric parameters to define and control the spatial interaction between nodes and collapse triggers in a bamboo-inspired crash box. This formulation provides a reproducible geometric procedure for determining the protection zone, the center-to-center distance between the node and the nearest void, and the axial distribution of voids based on the crash box's primary dimensions. The proposed formulation provides a geometric framework for linking the structural principles of bamboo to the control of the failure initiation location in thin-walled energy absorbers, while also providing a geometric basis for evaluating the influence of these local interactions on crashworthiness performance.

2 Materials and methods

Numerical simulations were performed using a parametric finite element analysis (FEA) approach to evaluate the effect of the node protection zone coefficient K_z on the crashworthiness response of the crash box. For all configurations, the material properties, primary dimensions, loading conditions, and other numerical parameters were kept constant, while the value of K_z was varied to 0.03, 0.05, and 0.07. This setup is used to isolate the effects of changes in geometric parameters on the structural response. A similar design-variable-based FEA approach was reported by Putra et al. [23], who systematically evaluated variations in structural design parameters to assess their effects on structural response.

2.1 Biomimetic void trigger calculation

To maintain the biomimetic node's function as a deformation arrestor while ensuring that the void trigger remains outside the node's direct influence zone, this study employs a dimensionless parameter-based approach to determine the axial distribution of voids. This approach is designed so that the position of the void is not determined arbitrarily, but is systematically derived from the crash box diameter, the node position, the void length, and the number of void rows.

2.1.1 Node protection zone

A node protection zone is established around the node's position to prevent voids from being placed too close to the node. The size of this zone is expressed as a function of the outer diameter of the crash box:

$$Z = K_z D \tag{1}$$

Where Z is the size of the node protection zone (mm), D is the outer diameter of the crash box (mm), and K_z is the dimensionless node protection zone coefficient. In this study, K_z was evaluated at three candidate values: 0.03, 0.05, and 0.07. With a crash box diameter of D = 75, the following results were obtained:

Table 1. Geometric determination of the node protection zone and its positional parameters

K_z	$Z\ (mm)$	Lower Node Position Limit (mm)	Upper Node Position Limit (mm)	$\mathrm{dc(mm)}$
0.03	2.25	37.75	42.25	8.50
0.05	3.75	36.25	43.75	11.50
0.07	5.25	34.75	45.25	14.50

The K_z value is treated as a design parameter evaluated numerically, rather than as a universal constant established in the literature. The final value is selected based on the results of a preliminary study of crashworthiness response and node integrity.

2.1.2 Node protection boundaries

If B represents the center position of the node measured from the end of the crash box, then the lower and upper boundaries of the node protection zone can be expressed as follows:

$$y_{NPZ}^{-} = B - Z \tag{2}$$

$$y_{NPZ}^{+} = B + Z \tag{3}$$

Therefore, the regions that the void center must avoid are:

$$B - Z < y_v < B + Z \tag{4}$$

where y_v denotes the axial position of the void center. For $B = 40\ mm$:

2.1.3 Node- to-Void Center Clearance

Since the size of a void cannot be represented solely by its center point, the distance between the node center and the void center must take into account half the length of the void. Therefore, this study establishes the parametric node-to-void center clearance rule as follows:

$$d_c = 2Z + \frac{L_v}{2} \tag{5}$$

Where:

- d_c = axial distance from the center of the node to the center of the nearest void (mm);
- Z = *node protection zone* (mm);
- L_v = total length of the void (*end-to-end length*) (mm).

For L_v= 8 mm, we obtain

2.1.4 Available upper and lower internode regions

Once the node region and the node-to-void distance have been determined, the void region is divided into two regions: the region above the node and the region below the node. For the n_u rows of the void region above the node, the axial position of each row is calculated using:

$$y_{u,i} = \frac{i}{n_u}(B - d_c), \quad i = 1,2, \dots, n_u \tag{6}$$

Where:

- $y_{u,i}$= the axial position of the i-th void row above the node;
- n_u = number of void rows in the upper region
- B = central node position
- d_c = distance between the center of a node and the center of a void.

For a total of four rows, two rows are placed above the node, so n_u= 2

2.1.5 Void positions below the node

Table 2. Circumferential distribution and alternating angular arrangement of void triggers for different node protection coefficients

K_z	Void Row	Axial Position (mm)	Void Pattern	Model
0.03	$y_{u,1}$	$\frac{1}{2}(40 - 8.5) = 15.75$	Normal	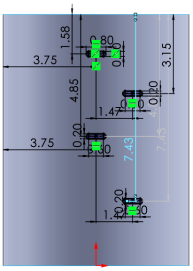
	$y_{u,2}$	$\frac{2}{2}(40 - 8.5) = 31.50$	Staggered	
	$y_{l,1}$	$40 + 8.5 = 48.5$	Normal	
	$y_{l,2}$	$48.5 + \frac{1}{2}(100 - 48.5) = 74.25$	Staggered	
0.05	$y_{u,1}$	$\frac{1}{2}(40 - 11.5) = 14.25$	Normal	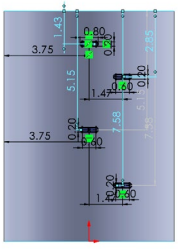
	$y_{u,2}$	$\frac{2}{2}(40 - 11.5) = 28.50$	Staggered	
	$y_{l,1}$	$40 + 11.5 = 51.5$	Normal	
	$y_{l,2}$	$51.5 + \frac{1}{2}(100 - 51.5) = 75.75$	Staggered	
0.07	$y_{u,1}$	$\frac{1}{2}(40 - 14.5) = 12.75$	Normal	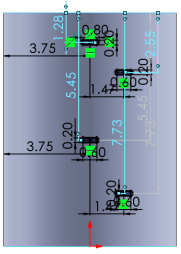
	$y_{u,2}$	$\frac{2}{2}(40 - 14.5) = 25.50$	Staggered	
	$y_{l,1}$	$40 + 14.5 = 54.5$	Normal	
	$y_{l,2}$	$54.5 + \frac{1}{2}(100 - 54.5) = 77.25$	Staggered	

For the area below the node, the positions of the void rows are determined by dividing the available area evenly:

$$y_{l,j} = (B + d_c) + \frac{j-1}{n_l}\,[H - (B + d_c)], \quad j = 1,2, \dots, n_l \tag{7}$$

Where:

- $y_{l,j}$= posisi aksial baris void ke-j di bawah node; the axial position of the j-th void row below the node;
- n_l = number of empty rows in the lower region
- H = Total height of the crash box

For a 4-row configuration n_l= 2. Equations (6) and (7) yield a mathematically determined axial distribution, so the positions of the voids do not need to be determined individually on a subjective basis.

2.2 Crash box geometry configuration

Five crash box geometric configurations were developed to investigate the effect of the node protection zone on axial crushing performance, as shown in Figure 1. All configurations shared a cylindrical geometry with an outer diameter of $D = 75\ mm$, a height of $H = 100\ mm$, and uniform wall thickness of 1 mm. The model configurations were designed based on three main geometric parameters: node position (B), biomimetic void trigger density (C), and node protection zone coefficient (K_z). Parameter B indicates the position of the node measured from the impact end of the crash box; thus, B40 indicates the position of the node at a distance of 40 mm from the impact end. Parameter C indicates the number of rows of biomimetic void triggers; thus, C4 indicates a configuration with four rows of void triggers. Parameter Z specifies the value of K_z, with Z03, Z05, and Z07 representing K_z =0,03, 0,05, and 0,07 respectively. Based on the relationship $Z = K_z D$, the widths of the node protection zones used are 2,25, 3,75, and 5,25 mm, for Z03, Z05, dan Z07 respectively. The three main configurations, B40-C4-Z03, B40-C4-Z05, and B40-C4-Z07, maintain the same node position and void-trigger configuration, while K_z is varied to isolate the effect of the node protection zone.. The C4-Z05 configuration was used as a comparison to evaluate the effect of the presence of a node at K_z = 0,05, while the Tube was used as a reference structure without biomimetic features. All subsequent configurations were analyzed using the same material properties, loading conditions, boundary conditions, and numerical parameters so that differences in mechanical response could be attributed to the geometric variations under study.

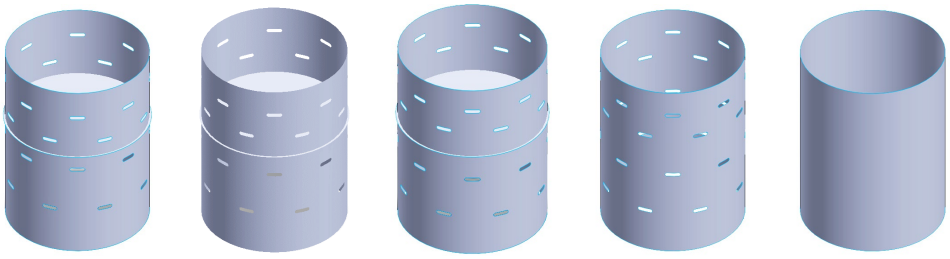

(a) (b) (c) (d) (e)

Fig. 1. Crash Box Geometric Configurations: (a) B40-C4-Z03, (b) B40-C4-Z05, (c) B40-C4-Z07, (d) C4-Z05, and (e) Plain Tube

2.3 Material model

The Johnson–Cook material parameters for heat-treated AlSi10Mg were adopted from the literature, with an initial yield stress of 118.24 MPa, a hardening constant of 60 MPa, and a hardening exponent of 0.35. The strain-rate constant was set to zero, excluding strain-rate effects from the constitutive response, while the reference strain rate was specified as 1 s^{-1}. The thermal softening exponent and melting temperature were set to 1 and 570 °C, respectively.

2.4 Numerical validation

To ensure the reliability and convergence of the numerical framework, the baseline finite element model configuration was validated against empirical data from quasi-static axial crushing tests of additively manufactured, heat-treated AlSi10Mg circular straight tubes available in the [24]. The experimental benchmark established an initial peak force of 51.5 kN and a mean crushing force of 32 kN. The current numerical formulation yields a representative force-displacement oscillation and successfully captures the characteristic over-stiffening effect 87.64 typical of ideal boundary conditions in explicit dynamic solvers. This minor discrepancy is non-critical and falls within the acceptable margin for structural crashworthiness analysis, as it ignores stochastic printing defects such as micro-porosity.

2.5 Mesh quality assessment

The mesh quality of all configurations was evaluated using the Element Quality metric in Ansys Workbench, yielding a consistent average range of 0.86390 to 0.99642, with minimum values spanning 0.28179 to 0.63645 (Table 3). To ensure spatial discretization independence, a grid convergence study was concurrently integrated using three refinement levels (Coarse: M1, Medium: M2, and Fine: M3) for the representative B40-C4-Z05 configuration. While the transition from M1 to M2 altered Energy Absorption (EA) by 8.23%, the variance asymptotically stabilized between M2 and M3 with a marginal EA discrepancy of merely 0.81% and converged load responses. Consequently, the B40-C4-Z05 M3 configuration was strictly selected for subsequent explicit dynamic simulations, guaranteeing full mesh-independent convergence and high computational fidelity without numerical locking.

Table 3. Element quality statistics for each configuration

Model	Min. Quality	Max. Quality	Average Quality	Standard Deviation (σ)
B40-C4-Z03	0.30268	0.99996	0.86783	0.12483
B40-C4-Z05	0.28528	0.99999	0.86787	0.12472
B40-C4-Z07	0.28179	0.99995	0.86750	0.12324
C4-Z05	0.28683	0.99999	0.86390	0.13069
Plain Tube	0.63645	0.99946	0.99642	0.01989

2.6 Impact loading and impactor model

The loading was performed using a cylindrical impactor with dimensions of 100 mm × 2 mm. The impactor was modeled as a rigid body with a mass of 103 kg. The impactor's initial velocity was set at 7.67 m/s and directed along the longitudinal axis of the crash box, resulting in an axial impact loading as shown in Figure 2. The explicit dynamic simulation was performed with an end time of 0.0119 s, which was defined as the time-based termination criterion for all configurations. Bonded contact was assigned to the designated interfaces, while general body interactions employed trajectory-based detection with a penalty formulation. Hourglass deformation was controlled using AUTODYN Standard damping with a viscous coefficient of 0.1. No friction coefficient was assigned to the bonded interfaces.

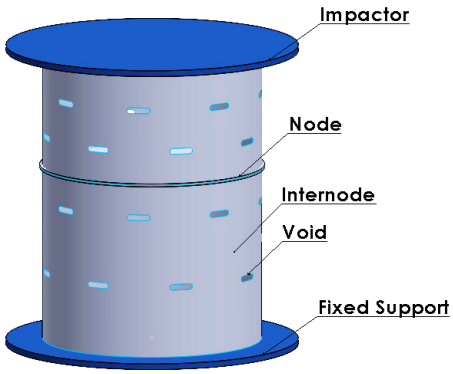

Fig. 2. Schematic representation of the biomimetic bamboo crash box and axial crushing configuration

2.7 Crashworthiness parameters

Crashworthiness performance was evaluated based on the force–displacement curve obtained from the simulation. The parameters analyzed included energy absorption (EA), initial peak force (IPF), mean crushing force (MCF), crush force efficiency (CFE), and specific energy absorption (SEA). EA was calculated based on the area under the force–displacement curve during the crushing process:

$$EA = \int_0^{\delta} F(x)dx \tag{8}$$

where $F(x)$ is the reaction force and δ is the crushing displacement.

The MCF is calculated as:

$$MCF = \frac{EA}{\delta} \tag{9}$$

Meanwhile, CFE is defined as:

$$CFE = \frac{MCF}{IPF} \tag{10}$$

and SEA is calculated based on:

$$SEA = \frac{EA}{m} \tag{11}$$

and m is the mass of the crash box structure used in the calculation.

3 Results and discussion

3.1 Force response and deformation characteristics

The force–reaction responses of the five crash-box configurations show distinct force characteristics during axial loading. The curves in Figure 3 show that all configurations experience changes in force throughout the crushing process, indicating a gradual progression of deformation and changes in the structure's resistance to axial shortening. Differences in response are particularly evident in the initial peak force, the progression of force during the crushing process, and the maximum force during the later stages of deformation. Visualizations of total deformation and equivalent von Mises stress also show that the configuration with biomimetic features produces different deformation

patterns and stress distributions compared to a plain tube. A similar approach to interpreting mechanical responses through load–displacement relationships and reaction forces has also been employed in finite element analyses of concrete slab structures with different material configurations. Such studies demonstrate how structural responses under loading can be compared using numerical outputs, including reaction forces, providing a methodological reference for interpreting mechanical responses in finite element-based investigations [25].

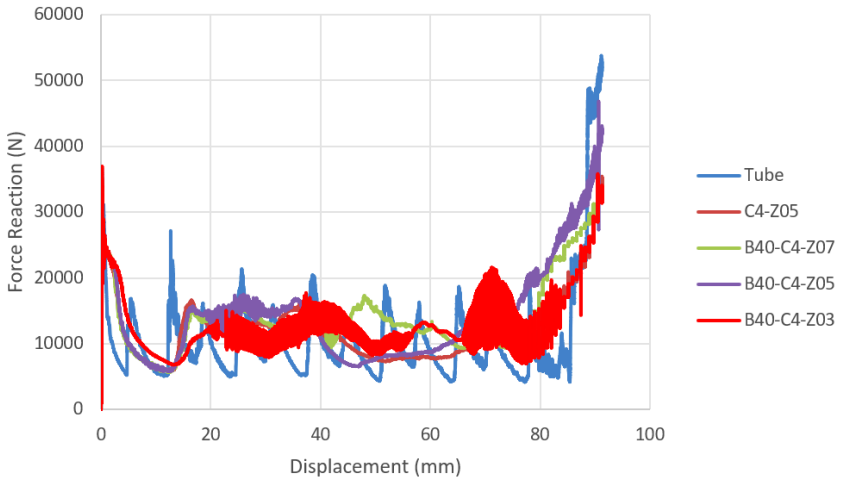

Fig. 3. Force–displacement responses of the investigated biomimetic bamboo crash box configurations under axial crushing

For the plain tube, the maximum reaction force reached 53,780 N, while the B40-C4-Z03, B40-C4-Z05, and B40-C4-Z07 configurations produced 36,956, 46,852, and 34,501 N, respectively. These values indicate that the presence of node features and biomimetic void triggers alters the structural force response compared to tube geometries without biomimetic features. In a biomimetic configuration, force fluctuations throughout the crushing process can be attributed to changes in the structure's resistance as local deformation develops in the wall sections. Thus, the force response is influenced not only by the initial structural stiffness but also by the sequence and location of deformation that develop during crushing.

The total deformation pattern shows that deformation in the biomimetic configuration does not develop uniformly along the height of the structure. Deformation is concentrated in several local regions and interacts with the presence of nodes and trigger voids. In contrast, the plain tube lacks these geometric features, so its deformation develops without a node–trigger interaction mechanism. These differences in patterns indicate that the geometric configuration plays a role in directing the development of deformation during axial loading. Visualization of the equivalent von Mises stress further reveals stress concentrations in regions undergoing local deformation, suggesting that the stress distribution can be used to explain the locations where plastic deformation occurs during the crushing process.

3.2 Effect of node protection zone on crashworthiness

The effect of the node protection zone was evaluated by comparing configurations B40-C4-Z03, B40-C4-Z05, and B40-C4-Z07. All three configurations maintained the same node positions and void trigger configurations, while the node protection zone coefficient K_z was varied to 0.03, 0.05, and 0.07, respectively. With a crash box diameter of 75 mm, these variations resulted in node protection zone widths of 2.25, 3.75, and 5.25 mm.

The results in Table 4 show that an increase in K_z from 0.03 to 0.05 increased energy absorption from 1,097.30 to 1,206.20 J, or by 9.93%. Over the same range, the mean crushing force increased from 12,022.18 to 13,215.30 N, or by 9.92%. The increase in both parameters indicates that the B40-C4-Z05 configuration is capable of maintaining a higher average crushing force during the deformation process, thereby resulting in a greater total energy absorption capacity. The influence of geometric variations on structural mechanical responses has also been demonstrated by Budi et al. [26], who investigated changes in flexural load capacity and load–deflection characteristics in cellular lightweight concrete panels with different thicknesses. Their findings provide general evidence that changes in structural dimensions can influence load-bearing responses, although the material characteristics and loading mechanisms differ from those of the crash box investigated in the present study. In the present study, this effect was examined by varying K_z, which alters the geometric relationship between the node and the void-trigger region during crushing.

Table 4. Crashworthiness performance of the investigated biomimetic bamboo crash box configurations under axial crushing

Model	Mass (gr)	EA (J)	FR max (N)	IPF (N)	MCF (N)	CFE (%)	SEA (J.kg^-1)
B40-C4-Z03	74.046	1,097.30	36,956.00	36,956.00	12,022.18	32.52	14,819.17
B40-C4-Z05	74.046	1,206.20	46,852.00	35,307.00	13,215.30	37.42	16,289.87

Model	Mass (gr)	EA (J)	FR max (N)	IPF (N)	MCF (N)	CFE (%)	SEA (J.kg^-1)
B40-C4-Z07	74.046	1,192.40	34,501.00	34,501.00	13,064.10	37.87	16,103.50
C4-Z05	61.613	1,026.60	35,454.00	33,828.00	11,247.58	33.25	16,662.07
Plain Tube	62.910	916.33	53,780.00	36,658.00	10,039.44	27.39	14,565.73

The mass values varied among the investigated configurations because of differences in their geometric features. The three configurations incorporating the node protection zone (B40-C4-Z03, B40-C4-Z05, and B40-C4-Z07) had identical masses of 74.046 g. In comparison, the C4-Z05 and plain tube configurations had masses of 61.613 g and 62.910 g, respectively. Reporting the mass to three decimal places provides sufficient numerical precision for examining the relationship between energy absorption (EA) and specific energy absorption (SEA).

The deformation pattern in B40-C4-Z05 indicates that changes in the width of the node protection zone affect the development of deformation around the node region. These changes not only alter the local dimensions of the structure but also modify the geometric interaction zone between the node and the void trigger region. The distribution of equivalent von Mises stress indicates that stress is concentrated in the parts of the structure undergoing local deformation. Thus, the increase in K_z to 0.05 can be attributed to changes in the deformation path and the distribution of structural resistance during crushing. This interpretation is consistent with the increase in mean crushing force and energy absorption observed for this configuration.

However, increasing K_z from 0,05 to 0,07 did not result in an improvement in all crashworthiness indicators. Energy absorption actually decreased slightly from 1,206.20 to 1,192.40 J, while the mean crushing force decreased from 13,215.30 to 13,064.10 N. Conversely, the initial peak force decreased from 35,307 to 34,501 N, and the crush force efficiency increased from 37.42% to 37.87%.

These changes indicate that the influence of the node protection zone on the evaluated crashworthiness parameters stabilizes beyond $K_z = 0.05$. Crucially, the minor reductions in energy absroption (1.1%) and mean crushing force (1.1%) from $K_z = 0.05$ to 0.07 fall close to the 0.81% grid convergence uncertainty established in Section 2.5. Therefore, these variations should be interpreted as a performance plateau governed by numerical sensitivity rather than a definitive degradation of structural capacity. Expanding the node protection zone beyond this range yields diminishing returns, suggesting a threshold where the structural interaction reaches a balance. Within the geometric range studied, changes in K_z affect the trade-off between the structure's ability to withstand crushing forces, control initial peak forces, and absorb energy. Thus, K_z can be regarded as a geometric parameter governing the interaction between nodes, which act as deformation-controlling elements, and void-trigger regions, where deformation is initiated.

3.3 Deformation pattern and von-Mises stress distribution

The deformation patterns and equivalent von Mises stress distributions shown in Figures 4 and 5 were used to interpret the progression of the collapse mechanism in each configuration. This approach allows changes in force response to be discussed not only in terms of crashworthiness values, but also in relation to the location and progression of local deformation within the structure. The use of deformation patterns and stress distributions to interpret collapse mechanisms has also been reported in parametric numerical studies of thin-walled structures and stiffened panels [4]. Figure 4 shows that the B40-C4-Z03, B40-C4-Z05, and B40-C4-Z07 configurations exhibited local deformation in several sections of the crash box wall, whereas the plain tube exhibited a deformation pattern without nodes or trigger voids. In the biomimetic configurations, these geometric features created local conditions that influenced the progression of deformation along the loading direction.

In B40-C4-Z03, the smaller node protection zone limits the geometric interaction region between the node and the surrounding deformation area. As K_z increases to 0.05, the node's influence region becomes larger, causing the deformation pattern around the node to exhibit a broader distribution. Changes in the width of the node protection zone not only alter the local dimensions of the structure but also change the geometric interaction region between the node and the void trigger area. These changes are reflected in the local deformation patterns and the distribution of equivalent von Mises stress that develop during the crushing process. These conditions correspond to the increase in mean crushing force and energy absorption observed in B40-C4-Z05. These results indicate that changes in the dimensions of the protection zone can influence the development of local deformation and, in turn, contribute to the global force response.

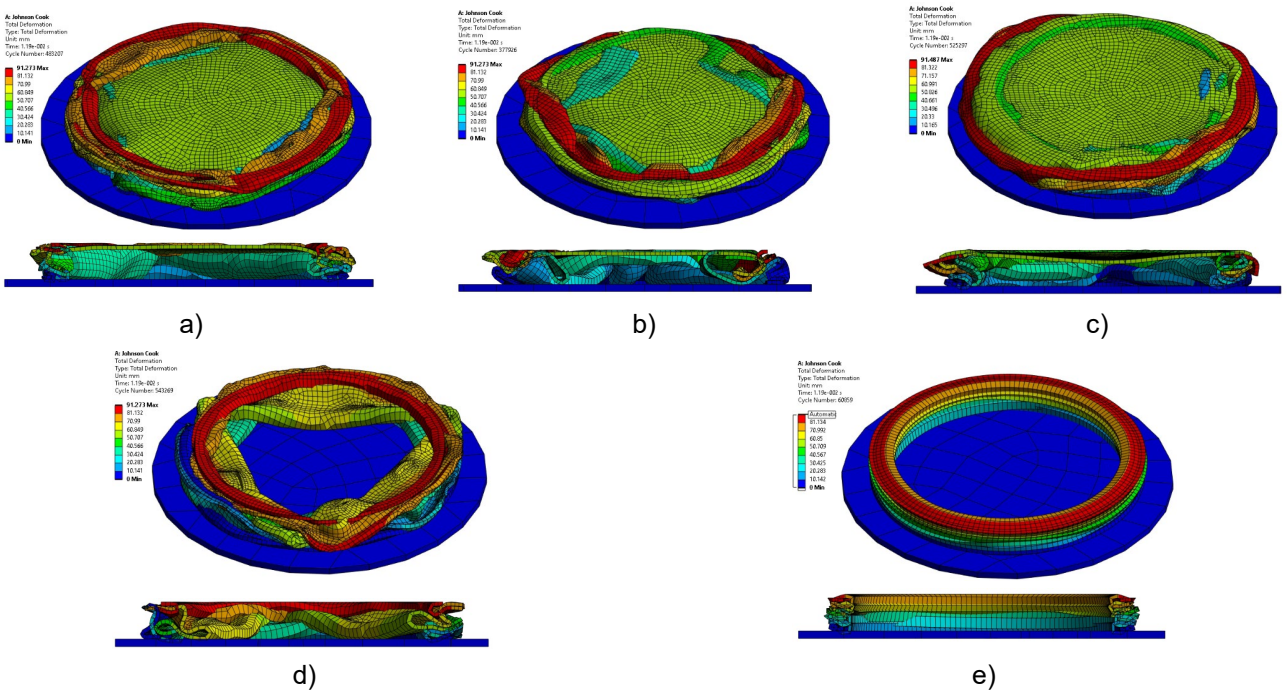

a) b) c) d) e)

Fig. 4. Total Deformation: (a) B40-C4-Z03, (b) B40-C4-Z05, (c) B40-C4-Z07, (d) C4-Z05, and (e) Plain Tube

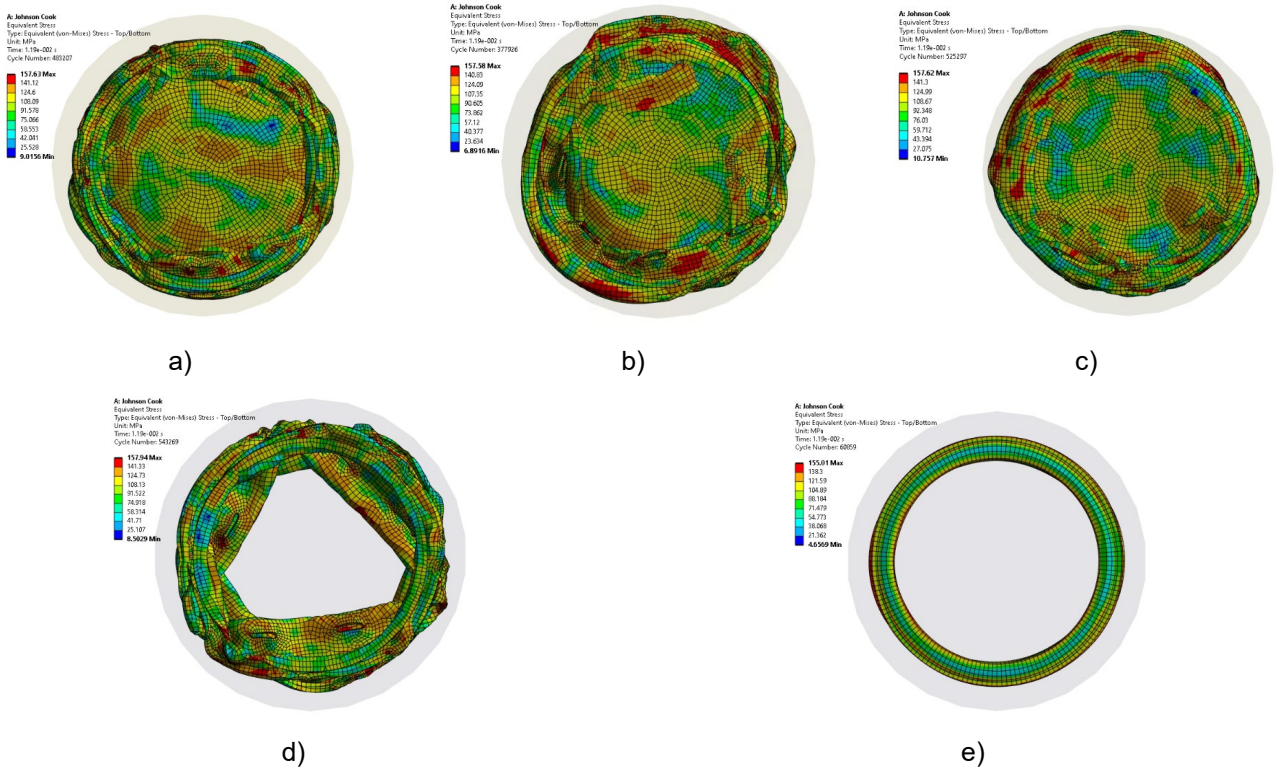

a) b) c) d) e)

Fig. 5. Equivalent Stress: (a) B40-C4-Z03, (b) B40-C4-Z05, (c) B40-C4-Z07, (d) C4-Z05, and (e) Plain Tube

At K_z = 0,07, further expansion of the node protection zone does not result in an increase in energy absorption. Instead, energy absorption decreased slightly compared with Z05. These findings indicate that the effect of nodes on deformation cannot be understood solely through an increase in the size of the protection zone. When the region is enlarged, the geometric interaction between the nodes and the collapse trigger areas also changes. Therefore, there are specific geometric conditions within the studied range that result in a balance between local deformation constraints and the structure's ability to undergo progressive plastic deformation.

The equivalent von Mises stress distribution shown in Figure 5 further supports this interpretation, indicating that stress concentrations are primarily localized in regions undergoing local deformation. In a biomimetic configuration, the locations of stress concentrations are associated with the node regions and the sections of the wall that undergo deformation, whereas the plain tube does not contain the node–protection-zone geometric mechanism.

In the context of this study, the Von Mises stress distribution was not used as the sole parameter for determining the configuration with the highest crashworthiness performance. Instead, the results were used to explain the relationship

between geometric configuration and deformation behavior. This approach is important because crashworthiness is determined by the overall response of the structure, as reflected by a combination of initial peak force, mean crushing force, energy absorption, crush force efficiency, and specific energy absorption.

3.4 Trade-off among crashworthiness indicators

A quantitative comparison shows that no single configuration achieved the highest values across all crashworthiness indicators. The B40-C4-Z05 configuration produced an energy absorption of 1,206.20 J and a mean crushing force of 13,215.30 N, which were the highest values among the three B40-C4 configurations. Meanwhile, B40-C4-Z07 produced an initial peak force of 34,501 N and a crush force efficiency of 37.87%, which were slightly lower and higher, respectively, than those of B40-C4-Z05.

These differences indicate a trade-off between energy absorption capacity and peak force control. B40-C4-Z05 produces higher EA and MCF values, but B40-C4-Z07 yields a lower IPF and a slightly higher CFE. Thus, increasing K_z from 0.05 to 0.07 provides benefits for certain indicators but does not improve overall energy absorption capacity. The differences in response among the parameters indicate that changes in K_z do not result in uniform improvements across all crashworthiness indicators. Therefore, configuration evaluation is not based on a single parameter, but takes into account a combination of energy absorption capacity, average crushing force, peak force, and energy absorption efficiency. Because the K_z variations did not produce uniform changes across all crashworthiness indicators, the configurations were evaluated using multiple performance measures rather than a single indicator. In structural and engineering system optimization, multi-objective approaches are commonly employed to evaluate multiple performance criteria that may involve competing requirements. For instance, Do et al. [27] applied multi-objective optimization to examine the balance between ride comfort and road-holding performance in an automotive air suspension system. This optimization principle is relevant to the present study, which considers multiple crashworthiness indicators to evaluate the trade-off between energy absorption capacity and peak-force response.

However, due to the limited number of evaluated K_z levels (three levels) and the proximity of the Z05 and Z07 variations to the numerical uncertainty bounds, these indicators represent a localized performance cluster rather than a global optimum. Within this evaluated range, B40-C4-Z05 exhibits a comparatively balanced response within the B40-C4 group, as it yields the highest EA and MCF while maintaining a lower IPF than Z03 and a CFE value close to that of Z07. This statement is not intended to establish Z05 as the superior configuration across all parameters, but rather to demonstrate that this configuration offers a balance between energy absorption capacity, average crushing force, and peak force control within the design range under study.

3.5 Comparison with the plain tube

To evaluate the overall contribution of the biomimetic features, the B40-C4-Z05 configuration was compared to a plain tube as a reference structure. The plain tube produced an energy absorption of 916.33 J, an initial peak force of 36,658 N, a mean crushing force of 10,039.44 N, a crush force efficiency of 27.39%, and a specific energy absorption of 14,565.73 J/kg. In contrast, B40-C4-Z05 produced 1,206.20 J, 35,307 N, 13,215.30 N, 37.42%, and 16,289.87 J/kg, respectively.

Compared to the plain tube, the B40-C4-Z05 increased energy absorption by 31.64% and the mean crushing force by 31.63%. Crush force efficiency increased from 27.39% to 37.42%, or by 36.62% in relative terms. The lowest crush force efficiency recorded by the Plain Tube (27.39%) matches the fundamental behavior of un-triggered thin-walled structures observed experimentally. In un-triggered configurations, the massive energy required to initiate the first plastic hinge generates an extreme asymmetric peak force relative to the average crushing resistance. This trend is mathematically consistent with benchmark experimental data of un-triggered AlSi10Mg tubes, where the absence of geometric triggers similarly constrained the structural efficiency, thereby validating the necessity of introducing the proposed biomimetic void trigger and node protection zones [24]. At the same time, the initial peak force decreased by 3.69%, from 36,658 to 35,307 N. A decrease was also observed in the maximum reaction force, from 53,780 N for the plain tube to 46,852 N for the B40-C4-Z05, or by 12.88%.

The simultaneous increase in EA and MCF, together with the decrease in IPF, indicates that the biomimetic configuration alters both the energy-absorption capacity and force-response characteristics of the structure during axial crushing. The deformation patterns and stress distributions obtained from the simulations support the interpretation that the node and void trigger features direct the progression of deformation toward specific regions, while the node protection zone governs the geometric interaction between the node region and the deformation initiation region.

Thus, the improvement in crashworthiness of the B40-C4-Z05 cannot be attributed solely to the presence of any single geometric feature. This response is the result of the interaction between the nodes, the biomimetic void trigger, and the node protection zone. In the context of the design under study, these results support the use of the node protection zone as a geometric parameter to control the progression of deformation and achieve a compromise between energy absorption capacity and force control during axial loading.

4 Conclusions

This study evaluates the effect of the node protection zone on the crashworthiness response of a biomimetic bamboo crash box through axial crash simulations. The node protection zone is defined as a dimensionless geometric

parameter via the coefficient K_z, with K_z = 0.03, 0.05, and 0.07, thereby enabling a systematic evaluation of the influence of the interaction zone between the node and the collapse-trigger region. The results show that changes in K_z affect the deformation pattern, stress distribution, force response, and energy absorption characteristics, and that these effects reach a performance plateau at higher protection widths. Within the design range studied, the B40-C4-Z05 configuration produced marginally higher values for energy absorption and mean crushing force compared to Z07, though the difference resides near the grid uncertainty limit. Overall, the findings of this study indicate that the range of $K_z = 0.05$ to 0.07 provides a relatively balanced compromise between energy absorption capacity, average crushing force, and peak force control within the range of configurations studied. Future studies incorporating a broader spectrum of intermediate K_z levels are required to definitively chart the transition boundaries. Between energy absorption capacity, average crushing force, and peak force control within the range of configurations studied. These findings do not yet indicate a global optimum, as the evaluation was limited to three values of K_z and the simulation conditions used. Future research should expand the range of the node protection zone and evaluate its interaction with wall thickness, node position, void trigger distribution, and material parameters; it should then validate the numerical results through experimental testing to assess the performance of the identified mechanisms under actual loading conditions.

5 Acknowledgements

The authors gratefully acknowledge the financial support provided through the Indonesian Education Scholarship (BPI), administered by the Center for Higher Education Funding and Assessment (PPAPT) and supported by the Indonesian Endowment Fund for Education (LPDP). This work was supported under the Decree of the Head of the Center for Higher Education Funding No. 01553/BPPT/BPI.06/9/2023. This support has provided a valuable opportunity to pursue doctoral studies and to contribute to the advancement of research and knowledge.

The author sincerely appreciates the commitment of these institutions to supporting the development of Indonesian scholars and doctoral research.

This paper was presented at the 12th International Conference and Exhibition on Sustainable Energy and Advanced Materials (ICE-SEAM 2026), held at Truntum Kuta, Bali, Indonesia, on 10-11 September 2026. It was subsequently submitted for consideration for publication in the Thematic section of the Journal of Applied Engineering Science associated with the conference. The paper was not published in the conference proceedings.

6 References

[1] Abdullah, N., Sani, M., Salwani, M., & Husain, N. (2020). A review on crashworthiness studies of crash box structure. *Thin-Walled Structures, 153*, 106795. https://doi.org/10.1016/j.tws.2020.106795

[2] Quan, V., Tam, T., Ngoc, N., & Hien, N. (2025). Application of the finite element method to investigate the impact of frontal collisions on the driver of a 29-seat passenger bus. *Journal of Applied Engineering Science, 23(3),* 575–586. https://doi.org/10.5937/jaes0-58487

[3] Baroutaji, A., Sajjia, M., & Olabi, A.-G. (2017). On the crashworthiness performance of thin-walled energy absorbers: Recent advances and future developments. *Thin-Walled Structures, 118,* 137–163. https://doi.org/10.1016/j.tws.2017.05.018

[4] Hanif, M., Adiputra, R., Prabowo, A., Muhayat, N., Marta, A., Huda, N., & Carvalho, H. (2023). Effect of design parameters on the ultimate strength and collapse behaviour of stiffened panels. *Journal of Applied Engineering Science, 21(3),* 940–956. https://doi.org/10.5937/jaes0-44738

[5] Fu, J., Liu, Q., Ma, X., & Cai, M. (2024). Energy absorption characteristics of bio-inspired multi-corner CFRP tubes under axial quasi-static and dynamic loading. *Thin-Walled Structures, 205,* 112551. https://doi.org/10.1016/j.tws.2024.112551

[6] Liu, K., Yu, Z., Wang, K., & Jing, L. (2022). Crashworthiness of bamboo-inspired circular tubes used for the energy absorber of rail vehicles. *Acta Mechanica Sinica, 38(8)*, Article 122014. https://doi.org/10.1007/s10409-022-22014-9

[7] Zuhri, M., Liao, Y., Wang, Q., & Guan, Z. (2019). The energy absorbing properties of bamboo-based structures. *Journal of Sandwich Structures & Materials, 21(3),* 1032–1054. https://doi.org/10.1177/1099636217707171

[8] Chen, X., Wang, X., Shang, L., Ma, X., Fang, C., Fei, B., Liu, H., & Zhang, S. (2024). Three-dimensional structural characterization and mechanical properties of bamboo parenchyma tissue. *Industrial Crops and Products, 208,* 117833. https://doi.org/10.1016/j.indcrop.2023.117833

[9] Hu, D., Wang, Y., Song, B., Dang, L., & Zhang, Z. (2019). Energy-absorption characteristics of a bionic honeycomb tubular nested structure inspired by bamboo under axial crushing. *Composites Part B: Engineering, 162,* 21–32. https://doi.org/10.1016/j.compositesb.2018.10.095

[10] Song, J. F., Xu, S. C., Wang, H. X., Wu, X. Q., & Zou, M. (2018). Bionic design and multi-objective optimization for variable wall thickness tube inspired bamboo structures. *Thin-Walled Structures, 125,* 76–88. https://doi.org/10.1016/j.tws.2018.01.010

[11] Liang, H., Hao, W., Sun, H., Pu, Y., Zhao, Y., & Ma, F. (2022). On design of novel bionic bamboo tubes for multiple compression load cases. *International Journal of Mechanical Sciences, 218,* 107067. https://doi.org/10.1016/j.ijmecsci.2022.107067

[12] Zou, M., Song, J., Xu, S., Liu, S., & Chang, Z. (2018). Bionic design of the bumper beam inspired by the bending and energy absorption characteristics of bamboo. *Applied Bionics and Biomechanics, 2018*, 1–12. https://doi.org/10.1155/2018/8062321

[13] Liang, R., Xu, F., Zhu, Y., Liu, X., Mo, L., & Liu, N. (2024). Dynamic response of bionic non-convex tubes with proportional distribution of bulkhead. Proceedings of the Institution of Mechanical Engineers, Part C: *Journal of Mechanical Engineering Science, 238(10),* 4713–4727. https://doi.org/10.1177/09544062231204536

[14] Kulkarni, S. M., Mali, K. D., Kulkarni, D. M., & Thiruselvam, N. I. (2024). Novel thermo-mechanical triggers processed by friction stir to enhance the crashworthiness of an automobile crash-box. *Engineering Failure Analysis, 162*, 108416. https://doi.org/10.1016/j.engfailanal.2024.108416

[15] Niknejad, A., Abedi, M. M., Liaghat, G. H., & Zamani Nejad, M. (2012). Prediction of the mean folding force during the axial compression in foam-filled grooved tubes by theoretical analysis. *Materials & Design, 37,* 144–151. https://doi.org/10.1016/j.matdes.2011.12.032

[16] Yang, W., Peng, B., & Yang, K. (2025). Multi-objective optimization of diaphragm reinforced bamboo-inspired energy absorption systems. *Composite Structures, 356,* 118865. https://doi.org/10.1016/j.compstruct.2025.118865

[17] Hussain, N. N., Regalla, S. P., & Rao, Y. V. D. (2017). Comparative study of trigger configuration for enhancement of crashworthiness of automobile crash box subjected to axial impact loading. *Procedia Engineering, 173,* 1390–1398. https://doi.org/10.1016/j.proeng.2016.12.198

[18] Wang, X., Qin, R., & Chen, B. (2022). Crushing analysis under multiple impact loading cases for novel tailored-property multi-wall tubes. *International Journal of Crashworthiness, 27(4),* 1092–1110. https://doi.org/10.1080/13588265.2021.1909837

[19] Lv, J., Bai, Z., Du, X., Zhu, F., Chou, C. C., Jiang, B., & Xu, S. (2023). Crashworthiness design of 3D lattice-structure filled thin-walled tubes based on data mining. *International Journal of Crashworthiness, 28(3),* 435–448. https://doi.org/10.1080/13588265.2022.2101306

[20] Hwang, Y.-H., & Han, J.-H. (2024). Energy absorption optimisation of an origami-shaped crash box under axial loading. *International Journal of Crashworthiness, 29(1),* 132–141. https://doi.org/10.1080/13588265.2023.2196909

[21] Kusyairi, I., Choiron, M. A., Purnowidodo, A., & Bintarto, R. (2025). Optimizing Miura origami for enhanced energy absorption: A multi-objective approach. *Journal of Engineering Sciences, 12(2),* D25–D44. https://doi.org/10.21272/jes.2025.12(2).d3

[22] Li, P., & Xiao, J. (2024). Crashworthiness design and multi-objective optimization of bionic thin-walled hybrid tube structures. *Computer Modeling in Engineering & Sciences, 139(1),* 999–1016. https://doi.org/10.32604/cmes.2023.044059

[23] Putra, G., Fahryansyah, M., Riadi, A., Budiyanto, M., & Nugroho, F. (2025). Simplifying ship structural optimization through stress-based material selection. *Journal of Applied Engineering Science, 23(2)*, 191–197. https://doi.org/10.5937/jaes0-46616

[24] Mohamed, A. S., Laban, O., Tarlochan, F., Al Khatib, S. E., Matar, M. S., & Mahdi, E. (2019). Experimental analysis of additively manufactured thin-walled heat-treated circular tubes with slits using AlSi10Mg alloy by quasi-static axial crushing test. *Thin-Walled Structures, 138,* 10–22. https://doi.org/10.1016/j.tws.2019.02.022

[25] Wang, Y., Syamsunur, D., Memon, Z., Sultan, B., & Oksri, N. (2025). Performance of concrete slabs with waste materials: A study using finite element analysis. *Journal of Applied Engineering Science, 23(3),* 437–455. https://doi.org/10.5937/jaes0-55983

[26] Budi, G., Sutandar, E., Prasetijo, J., & Parabi, A. (2025). Sustainability analysis of lightweight concrete technologies: Optimizing CLC panel thickness for structural performance and environmental footprint reduction. *Journal of Applied Engineering Science, 23(3),* 558–574. https://doi.org/10.5937/jaes0-58360

[27] Do, T., Pham, T., Nguyen, T., Sename, O., & Vu, V. (2026). Multi-objective optimization with genetic algorithm of air suspension system for enhancing ride comfort and road-holding performances. *Journal of Applied Engineering Science, 24(2),* 367–377. https://doi.org/10.5937/jaes0-63429

7 Conflict of interest statement

The authors declare that they have no conflict of interest that could have influenced the research, analysis, or interpretation of the results presented in this manuscript.

8 Author contributions

Johan Wayan Dika: conceptualization, methodology, investigation, numerical simulation, formal analysis, visualization, and writing—original draft. Moch. Agus Choiron: conceptualization, methodology, supervision,

validation, and writing—review and editing. Putu Hadi Setyarini: methodology, investigation, numerical analysis, and writing—review and editing. Teguh Dwi Widodo: methodology, investigation, material analysis, and writing—review and editing. Yudhi Ariadi: writing—review and editing.

9 Data availability statement

The data supporting the findings of this study, including the numerical simulation results, are available from the corresponding author upon reasonable request.

10 Supplementary materials

No supplementary materials are provided for this study.

Paper submitted: 29.09.2026.
Paper accepted: 10.11.2026.
This is an open access article distributed under the CC BY 4.0 terms and conditions